

# **Mechanisms of Dynamic Deformation and Dynamic Failure in Aluminum Nitride**

**by Guangli Hu, C. Q. Chen, K. T. Ramesh, and J. W. McCauley**

**ARL-RP-375**

**June 2012**

**A reprint from *Acta Materialia*, Vol. 60, pp. 3480–3490, 2012.**

## **NOTICES**

### **Disclaimers**

The findings in this report are not to be construed as an official Department of the Army position unless so designated by other authorized documents.

Citation of manufacturer's or trade names does not constitute an official endorsement or approval of the use thereof.

Destroy this report when it is no longer needed. Do not return it to the originator.

# **Army Research Laboratory**

Aberdeen Proving Ground, MD 21005-5066

---

**ARL-RP-375****June 2012**

---

## **Mechanisms of Dynamic Deformation and Dynamic Failure in Aluminum Nitride**

**Guangli Hu, C. Q. Chen, K. T. Ramesh, and J. W. McCauley**  
**Weapons and Materials Research Directorate, ARL**

A reprint from *Acta Materialia*, Vol. 60, pp. 3480–3490, 2012.

REPORT DOCUMENTATION PAGE				Form Approved OMB No. 0704-0188	
Public reporting burden for this collection of information is estimated to average 1 hour per response, including the time for reviewing instructions, searching existing data sources, gathering and maintaining the data needed, and completing and reviewing the collection information. Send comments regarding this burden estimate or any other aspect of this collection of information, including suggestions for reducing the burden, to Department of Defense, Washington Headquarters Services, Directorate for Information Operations and Reports (0704-0188), 1215 Jefferson Davis Highway, Suite 1204, Arlington, VA 22202-4302. Respondents should be aware that notwithstanding any other provision of law, no person shall be subject to any penalty for failing to comply with a collection of information if it does not display a currently valid OMB control number. <b>PLEASE DO NOT RETURN YOUR FORM TO THE ABOVE ADDRESS.</b>					
1. REPORT DATE (DD-MM-YYYY) June 2012		2. REPORT TYPE Reprint		3. DATES COVERED (From - To) January 2009–December 2011	
4. TITLE AND SUBTITLE Mechanisms of Dynamic Deformation and Dynamic Failure in Aluminum Nitride				5a. CONTRACT NUMBER W911NF-06-02-0006	
				5b. GRANT NUMBER	
				5c. PROGRAM ELEMENT NUMBER	
6. AUTHOR(S) Guangli Hu,* C. Q. Chen,* K. T. Ramesh,* and J. W. McCauley				5d. PROJECT NUMBER BH 64	
				5e. TASK NUMBER	
				5f. WORK UNIT NUMBER	
7. PERFORMING ORGANIZATION NAME(S) AND ADDRESS(ES) U.S. Army Research Laboratory ATTN: RDRL-WM Aberdeen Proving Ground, MD 21005-5066				8. PERFORMING ORGANIZATION REPORT NUMBER ARL-RP-375	
9. SPONSORING/MONITORING AGENCY NAME(S) AND ADDRESS(ES)				10. SPONSOR/MONITOR'S ACRONYM(S)	
				11. SPONSOR/MONITOR'S REPORT NUMBER(S)	
12. DISTRIBUTION/AVAILABILITY STATEMENT Approved for public release; distribution is unlimited.					
13. SUPPLEMENTARY NOTES A reprint from <i>Acta Materialia</i> , Vol. 60, pp. 3480–3490, 2012. *Department of Mechanical Engineering, Johns Hopkins University, Baltimore, MD 21218					
14. ABSTRACT Uniaxial quasi-static, uniaxial dynamic and confined dynamic compression experiments have been performed to characterize the failure and deformation mechanisms of a sintered polycrystalline aluminum nitride using a servohydraulic machine and a modified Kolsky bar. Scanning electron microscopy and transmission electron microscopy (TEM) are used to identify the fracture and deformation mechanisms under high rate and high pressure loading conditions. These results show that the fracture mechanisms are strong functions of confining stress and strain rate, with transgranular fracture becoming more common at high strain rates. Dynamic fracture mechanics and micromechanical models are used to analyze the observed fracture mechanisms. TEM characterization of fragments from the confined dynamic experiments shows that at higher pressures dislocation motion becomes a common dominant deformation mechanism in AlN. Prismatic slip is dominant, and pronounced microcrack–dislocation interactions are observed, suggesting that the dislocation plasticity affects the macroscopic fracture behavior in this material under high confining stresses.					
15. SUBJECT TERMS dynamic deformation, failure, AlN, aluminum nitride, sintering, fracture, micromechanical modeling, dislocations					
16. SECURITY CLASSIFICATION OF:			17. LIMITATION OF ABSTRACT  UU	18. NUMBER OF PAGES  20	19a. NAME OF RESPONSIBLE PERSON J. W. McCauley
a. REPORT Unclassified	b. ABSTRACT Unclassified	c. THIS PAGE Unclassified			19b. TELEPHONE NUMBER (Include area code) 410-306-0711

# Mechanisms of dynamic deformation and dynamic failure in aluminum nitride

Guangli Hu<sup>a</sup>, C.Q. Chen<sup>a</sup>, K.T. Ramesh<sup>a,\*</sup>, J.W. McCauley<sup>b</sup>

<sup>a</sup> Department of Mechanical Engineering, Johns Hopkins University, Baltimore, MD 21218, USA

<sup>b</sup> U.S. Army Research Laboratory, Aberdeen Proving Ground, MD 21078, USA

Received 16 January 2012; accepted 5 March 2012

## Abstract

Uniaxial quasi-static, uniaxial dynamic and confined dynamic compression experiments have been performed to characterize the failure and deformation mechanisms of a sintered polycrystalline aluminum nitride using a servohydraulic machine and a modified Kolsky bar. Scanning electron microscopy and transmission electron microscopy (TEM) are used to identify the fracture and deformation mechanisms under high rate and high pressure loading conditions. These results show that the fracture mechanisms are strong functions of confining stress and strain rate, with transgranular fracture becoming more common at high strain rates. Dynamic fracture mechanics and micromechanical models are used to analyze the observed fracture mechanisms. TEM characterization of fragments from the confined dynamic experiments shows that at higher pressures dislocation motion becomes a common dominant deformation mechanism in AlN. Prismatic slip is dominant, and pronounced microcrack–dislocation interactions are observed, suggesting that the dislocation plasticity affects the macroscopic fracture behavior in this material under high confining stresses.

© 2012 Acta Materialia Inc. Published by Elsevier Ltd. All rights reserved.

**Keywords:** Sintering; Fracture; Deformation; Micromechanical modeling; Dislocations

## 1. Introduction

Aluminum nitride, with the commonly found wurtzite structure, is in the 6 mm point group, with lattice parameters of  $a = 0.311$  nm,  $c = 0.498$  nm and  $c/a = 1.6$  [1]. For single-crystal AlN, five independent elastic constants have been measured by nanoindentation [2] and vibrational spectroscopy [3]. Polycrystalline AlN, as shown in Fig. 1a, has also received attention because it is potentially a structural material for electronic substrates, thermal coatings, etc. There are two approaches to the production of bulk aluminum nitride: liquid phase pressureless sintering (“sintered AlN”) and hot pressing (“hot-pressed AlN”). Sintered AlN generally contains a second phase, as shown in Fig. 1b, which is a sintering aid,  $Y_2O_3$ , that provides rapid densification without external pressure [4]. AlN is

also considered as a potential armor material because of its interesting mechanical properties. Understanding the failure and deformation mechanisms in AlN under a range of strain rates and stress states is key for these applications.

Heard and Cline [5] performed low strain rate confined experiments on hot-pressed AlN and observed a brittle to ductile transition at a circumferential confining stress of 0.55 GPa; that transition was attributed to intracrystalline slip. Perfect dislocations with a Burgers vector of  $\frac{a}{3}\langle 11\bar{2}0 \rangle$  have been observed in AlN [1], usually dissociated into  $\frac{a}{3}\langle 10\bar{1}0 \rangle$  and  $\frac{a}{3}\langle 01\bar{1}0 \rangle$  in the basal plane. The spacing of the dissociated dislocations was around 8 nm [1]. Two possible glide planes were proposed and partial dislocations and stacking faults in AlN were observed by transmission electron microscopy (TEM) in the 1960s [6,7]. Dissociated dislocations have also been observed after Vickers indentation [8] and quasi-static confined tests using a Griggs-type apparatus in an Instron frame (at a strain rate of  $2 \times 10^{-5} s^{-1}$  and a confining pressure above 0.7 GPa) [9–11].

\* Corresponding author. Tel.: +1 410 516 7735; fax: +1 410 516 7254.  
E-mail address: [ramesh@jhu.edu](mailto:ramesh@jhu.edu) (K.T. Ramesh).

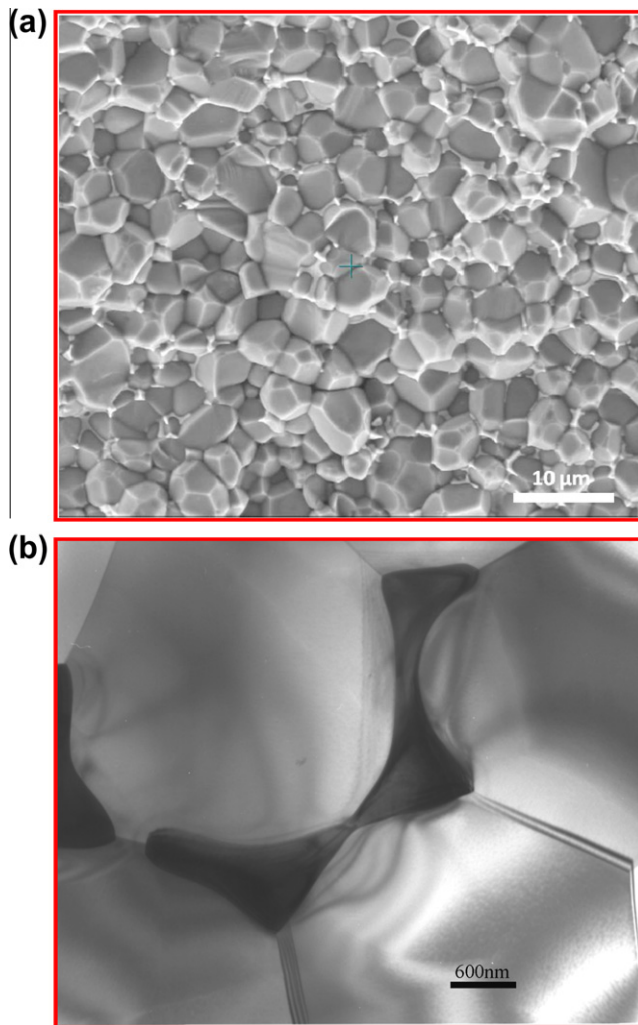


Fig. 1. (a) Field emission SEM of a cleaned fractured surface of polycrystalline sintered AlN (the white phase is yttrium oxide and the grey phase is AlN grains). (b) TEM micrograph of as-received sintered AlN (the dark region is the yttrium oxide phase and the grey region is AlN). Note the lack of dislocations in the grains, and the clean grain boundaries in some regions.

Dynamic confined experiments (with strain rates up to  $10^3 \text{ s}^{-1}$  and a confining stress up to 230 MPa) were performed on sintered AlN by Chen and Ravichandran using shrink-fit confinement, and the compressive strength was seen to be sensitive to both confining stress and strain rate [12]. Hot-pressed AlN also demonstrated a strong rate sensitivity at higher strain rates ( $10^2$ – $10^3 \text{ s}^{-1}$ ) in similar experiments [13]. Higher pressures and higher strain rates (above  $10^5 \text{ s}^{-1}$ ) are achieved in shock experiments, and Rosenberg et al. [14] performed such experiments on hot-pressed AlN, observing that the Hugoniot elastic limit was 9.4 GPa. Analysis of shock experiments indicates that the shear strength of AlN is nearly independent of pressure at high pressures [14–16]. It has been suggested that this behavior might be due to plastic flow in AlN [17]. In recent work, Hu et al. [18] conducted quasi-static compression, uniaxial dynamic compression and confined dynamic compression experiments on AlN with real-time high-speed

visualization of the failure processes. They observed that the compressive strength of the sintered AlN was sensitive to strain rate over the strain rate range of  $10^{-3}$ – $10^3 \text{ s}^{-1}$ , consistent with previous experimental data. They also showed that all of the available experimental data on AlN at low pressures could be understood in terms of wing crack mechanics, and suggested that at high pressures the dislocation mechanism could be dominant.

The microscopic fracture mechanisms of aluminum nitride have been studied by several authors. Cleavage steps were observed after indentation on AlN films, but no cleavage planes were identified [19]. There is (to our knowledge) no specific data on the cleavage of single-crystal AlN. However, the wurtzite crystal structure is commonly known to cleave along  $(11\bar{2}0)$  and  $(10\bar{1}0)$  planes [20]. Polycrystalline AlN has additional fracture mechanisms introduced by the grain boundaries, grain boundary phases, texture, sintering additives such as  $\text{Y}_2\text{O}_3$  and process-induced defects. Highly oriented polycrystalline AlN with a low mass percentage of  $\text{Y}_2\text{O}_3$  shows more transgranular fracture than randomly oriented AlN with a high mass percentage of  $\text{Y}_2\text{O}_3$ , which shows more intergranular fracture [21]. For a given polycrystalline ceramic, however, the active fracture mechanisms also depend on experimental conditions, such as the rate of loading and the confining pressures. These dependences are not understood for advanced ceramics in general, and for AlN in particular.

To summarize, the deformation mechanisms of AlN have been characterized under quasi-static confined experiments, indentation and high temperature quasi-static experiments [10,11]. However, there is limited data from dynamic confined experiments [12,22] with high confining stresses and high strain rates. These are the conditions relevant to protection applications, and there has been little direct microstructural characterization to determine the deformation and fracture mechanisms under such conditions (aside from soft recovery experiments on alumina [23]). Further, the fracture mechanisms of AlN have not been studied and analyzed systematically with respect to loading rate and stress rate.

In this paper, we focus on the deformation and fracture mechanisms of sintered AlN as a function of confining stress and strain rate. Uniaxial quasi-static, uniaxial dynamic and confined dynamic experiments are analyzed. Scanning electron microscopy (SEM) is used to examine the fracture mechanisms active in each of these experiments. A theoretical analysis of fracture mechanism transition, which can be applied to other material systems, is provided to explain our observations. Finally, TEM is used to study the deformation mechanisms under various loading conditions.

## 2. Experimental procedures

The material investigated is a pressureless liquid phase sintered AlN, provided by the Dow Chemical, with 3 weight percentage of yttria ( $\text{Y}_2\text{O}_3$ ) as a sintering additive

[24]. The average grain size is 5  $\mu\text{m}$  with yttria occupying some of the grain boundaries, as shown in Fig. 1a, which is a micrograph of a cleaned fracture surface. The TEM micrograph in Fig. 1b shows a region where the second phase (the “interphase”) sits along some of the grain boundaries and triple junctions. Multiple locations of our as-received material have been examined, and all of our TEM micrographs indicate that the as-received material is free of dislocations.

The experimental techniques used have been discussed in detail in previous work [18]. Here we summarize the differences among the techniques in terms of loading rate and pressure achieved. Quasi-static uniaxial compression tests have typical strain rates on the order of  $10^{-3} \text{ s}^{-1}$  and the peak hydrostatic pressure of about 1.1 GPa. (Note that all unconfined experiments have, by definition, a hydrostatic stress which is 1/3 of the axial stress.) Dynamic uniaxial compression tests have typical strain rates on the order of  $10^3 \text{ s}^{-1}$  and hydrostatic pressures of around 1.3 GPa. The typical loading rate in our confined dynamic experiments [18] is also on the order of  $10^3 \text{ s}^{-1}$  and the hydrostatic pressure that can be developed is as high as 1.5 GPa. These three experimental techniques enable us to vary the strain rate and confining stress (and thus the pressure).

The primary experimental results obtained by Hu et al. [18] on the mechanical behavior were the following. First, the uniaxial compressive strength increases with strain rate, and real-time in situ photography revealed large scale fracture dominated by axial cracking. Second, the deviatoric strength of the material increases linearly with the hydrostatic pressure until a critical pressure is reached. Beyond this transition pressure, the deviatoric strength is essentially independent of the hydrostatic pressure. These experimental observations are related to specific deformation and failure mechanisms in this manuscript.

We now describe the active fracture and deformation mechanisms in AlN, and discuss how the loading parameters affect these mechanisms.

### 3. Fracture mechanisms of sintered AlN

We have conducted extensive SEM-based analysis of the active fracture mechanisms. After each type of loading, multiple fragments and locations were examined to identify the fracture mechanisms. A thin layer of platinum was sputtered on the fragment surfaces to avoid charging and a representative number of fragments were examined.

#### 3.1. Definition of mechanism terminology

The sintered AlN material system is illustrated in Fig. 2a. “Grain failure” is defined as the fracture of grains (transgranular fracture). “Grain boundary failure” refers to grain–grain interface failure. “Grain–interphase failure” refers to the failure of the grain–yttria interface in regions where the  $\text{Y}_2\text{O}_3$  is present. “Interphase failure” is defined as the failure of the yttria itself. These four possible frac-

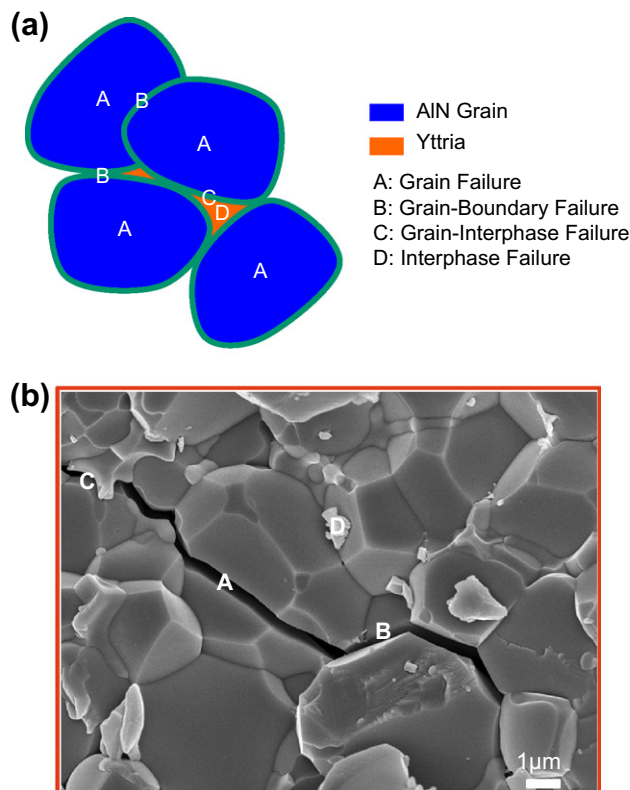


Fig. 2. (a) An illustration of the sintered AlN material system and related terminology definition. (b) All the active fracture modes after confined dynamic experiments (confining stress 780 MPa). A: transgranular fracture (grain failure); B: grain boundary failure; C: grain–interphase failure; D: interphase failure.

ture modes are representative of all sintered materials, as suggested by German [4]. Both grain boundary failure and grain–interphase failure are examples of so-called “intergranular fracture”. Note that our post-mortem analysis does not allow us to always distinguish grain boundary failure from grain–interphase failure from just one of the pair of fracture surfaces. In this paper, grain–interphase failure and grain boundary failure are treated together as intergranular fracture. Fig. 2b is an SEM image of a fracture surface obtained after a confined dynamic test, illustrating all the fracture modes described above. We describe the fracture mechanisms observed under each loading condition in what follows, and then analyze the fracture mechanism transition for this material.

#### 3.2. Observed fracture mechanisms

The fracture surfaces of fragments developed during quasi-static loading ( $\dot{\epsilon} \sim 10^{-3} \text{ s}^{-1}$ ) are shown in Fig. 3a, demonstrating primarily intergranular fracture. The cracks propagate along the grain boundaries: AlN grains bordering the crack path are almost completely intact and are just pulled out. For the quasi-static loading of our AlN, the intergranular failure mode is dominant and transgranular failure mode is only occasionally observed. Little or no interphase failure is observed. Such intergranular fracture



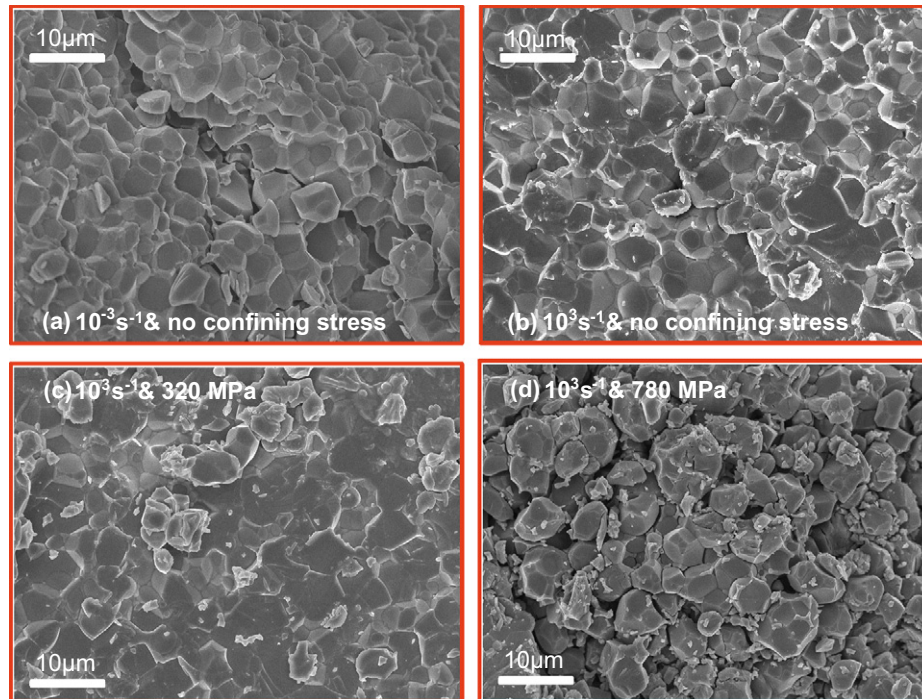


Fig. 3. Fracture surface comparison under different test conditions. (a) Quasi-static fracture surface, mainly intergranular fracture. (b) Uniaxial dynamic compression fracture surface, mainly transgranular fracture. (c) Confined dynamic compression fracture surface (320 MPa confining stress), mainly transgranular fracture with localized interphase failure. (d) Confined dynamic fracture surface (780 MPa confining stress), mainly transgranular fracture with more interphase failure.

is typical for general sintered materials, because the solid grain boundaries are typically weak. Similar dominance of intergranular fracture has also been observed in four point bending tests on spinel [25] and alumina [26] specimens. Fractography studies of alumina (Coors AD995) have shown that the area fraction of intergranular fracture was about 97% for statically loaded specimens [26].

Fig. 3b shows a typical fracture surface of fragments recovered after uniaxial dynamic compression ( $\dot{\epsilon} \sim 10^3 \text{ s}^{-1}$ ). A smoother fracture surface is observed, suggesting a higher percentage of transgranular fracture under dynamic loading compared with that under quasi-static loading. This observation agrees with in a hot-pressed AlN system after uniaxial dynamic experiments [13,27].

It seems to be a common trend, also suggested by numerical simulations in various brittle solids [28,29], that the percentage of transgranular fracture increases with an increase in loading rates. The area fraction of transgranular fracture of alumina varied from 3% to about 16% in quasi-static and impact-loaded specimens [26,30]. Similarly, fractography observations have shown that intergranular fracture dominates Al<sub>2</sub>O<sub>3</sub> specimens fractured under quasi-static loading, and inter/transgranular fracture dominates fracture under dynamic loading [31]. Note that a much higher transgranular fracture percentage was also observed in SiC<sub>w</sub>/Al<sub>2</sub>O<sub>3</sub> specimens under impact loading conditions [30]. All available evidence suggests that transgranular fracture becomes increasingly likely as the rate of loading increases, for reasons discussed in the following section. It appears that, once

a critical strain rate is achieved, transgranular fracture becomes dominant. Note that interphase failure is rarely observed in this material under these uniaxial compressive stresses.

The confined dynamic experiments (with strain rates on the order of  $10^3 \text{ s}^{-1}$ ) were performed with two superimposed confining stresses, 320 and 780 MPa [18]. Fig. 3c shows a typical fracture surface from the fragments recovered from confined dynamic experiments with 320 MPa confining stress (“low confinement”). Both intergranular and transgranular fracture are observed, but transgranular fracture is dominant. Interphase failure is also observed, though uncommon and quite localized. Note that interphase failure, which is the failure of the yttria itself when present along the grain boundaries or at triple junctions, is the distinctive fracture mode in sintered AlN systems.

Fragments from confined dynamic tests with a 780 MPa confining stress show failure patterns qualitatively similar to that observed in the 320 MPa confining stress case, but with increased interphase failure. Intergranular fracture, transgranular fracture and interphase failure are all observed, as shown in Fig. 3d. Transgranular fracture is still the dominant mechanism. However, the interphase failure mode is more common than for the 320 MPa confining stress level. This observation can also be understood with the micromechanical analysis presented below. The micrograph in Fig. 2b, which demonstrates the existence of all these fracture modes, is from a confined dynamic experiment with a 780 MPa confining stress.



## 4. Modeling the fracture mechanisms

### 4.1. Strain rate effects on fracture mechanisms

A major question that emerges from the experimental results concerns the underlying physics that drives the transition from intergranular to transgranular fracture as the loading rate increases. In what follows, we use dynamic fracture mechanics to analyze and predict this transition, considering the case of varying rate at fixed low pressures.

Since the transition is largely from intergranular (interfacial) fracture to transgranular fracture (crystallographic cleavage), these individual mechanisms must be examined in the context of this material. We note that the interfacial toughnesses of AlN–Y<sub>2</sub>O<sub>3</sub> and AlN–AlN interfaces are likely to be smaller than the toughnesses of both single-crystal AlN and Y<sub>2</sub>O<sub>3</sub>. This is generally the case for a sintered material [32,33], and is further demonstrated in this particular case by the intergranular fracture under quasi-static loading. The quasi-static interfacial toughness (not distinguishing the two kinds of interfaces) can be represented as  $\Gamma_c^{IT}$ , the quasi-static AlN toughness as  $\Gamma_c^{AlN}$  and the quasi-static Y<sub>2</sub>O<sub>3</sub> toughness as  $\Gamma_c^Y$ . Because of the low yttria volume fraction and since yttria failure is not observed under uniaxial loading, we ignore the explicit

Y<sub>2</sub>O<sub>3</sub> phase in the intergranular–transgranular transition. The competition is therefore viewed as being between the failure of the effective interfaces and the failure of the AlN grains.

The fracture scenario in our material system is illustrated in Fig. 4a. Consider a crack that is currently propagating along a grain boundary and that comes up towards another grain with an interfacial angle defined as  $\beta \in [0, \frac{\pi}{2}]$  as shown in Fig. 4a. The crack will propagate either along the interface (intergranular fracture) or into the grain (transgranular fracture), based on the maximum energy release rate in both the quasi-static and dynamic cases.

For the quasi-static case, we define  $G_s^{int}$  and  $G_s^{Tra}$  as the static energy release rates of the intergranular (deflecting) crack tip and the transgranular (penetrating) crack tip, respectively. Assuming that both  $G_s^{int}$  and  $G_s^{Tra}$  are higher than the corresponding fracture toughnesses  $\Gamma_c^{IT}$  and  $\Gamma_c^{AlN}$  for the propagating crack, the crack can develop into either intergranular or transgranular mode. The competition between intergranular and transgranular fracture is governed [34] by

$$\frac{G_s^{int}(\beta)}{G_s^{Tra}} \geq \frac{\Gamma_c^{IT}}{\Gamma_c^{AlN}} \quad (1a)$$

for intergranular fracture and

$$\frac{G_s^{int}(\beta)}{G_s^{Tra}} < \frac{\Gamma_c^{IT}}{\Gamma_c^{AlN}} \quad (1b)$$

for transgranular fracture. Note that, in this approximation, we are treating the material as a homogeneous solid and, on the left-hand side of Eqs. (1a) and (1b), the ratio of the two energy release rates  $G_s^{int}/G_s^{Tra}$  depends only on the interfacial angle  $\beta$ , while, on the right-hand side, the toughness ratio  $\Gamma_c^{IT}/\Gamma_c^{AlN}$  is a material property. If criterion (1a) is satisfied, the crack tends to develop into intergranular fracture. On the other hand, if criterion (1b) is satisfied, the crack tends to develop into transgranular fracture.

In Fig. 4b, the energy release rate ratio  $G_s^{int}/G_s^{Tra}$  and the quasi-static toughness ratio  $\Gamma_c^{IT}/\Gamma_c^{AlN}$  are plotted against the interfacial angle  $\beta$  as the dashed curved line and the horizontal cross-hatched line, respectively. As noted above, the interfacial toughness is typically much smaller than the toughness of the grain. Therefore, the quasi-static toughness ratio  $\Gamma_c^{IT}/\Gamma_c^{AlN}$  is taken to be less than 1 (arbitrarily set to 0.5 in the plot). If Eq. (1a) is satisfied, i.e. in the region where the dashed curved line is above the horizontal cross-hatched line in Fig. 4b, the crack tends to develop into an intergranular fracture mode. If we assume that the grain orientation is randomly distributed, whichever fracture mode covers a larger range of interfacial angle will be the dominant mode. Here, from Fig. 4b, we can see that the intergranular mode covers a larger range of interfacial angles if the quasi-static toughness ratio is less than 0.5 (as is typically the case), implying that the intergranular fracture is generally dominant. However, at very large interfacial angles, the transgranular

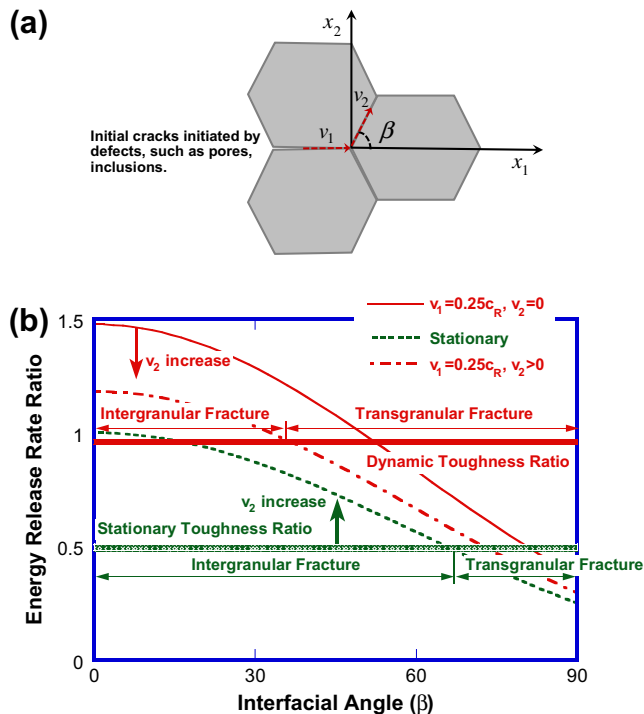


Fig. 4. (a) Illustration of the competition between intergranular and transgranular fracture mode. Initial cracks are generally initiated by the defects in the materials, such as pores and inclusions.  $v_1$  is the incoming crack velocity,  $v_2$  is the deflected interfacial crack velocity and  $\beta$  is the interfacial angle between the grain and grain boundary. (b) Energy release rate ratios plotted against the interfacial angle  $\beta$ . Note that the stationary and dynamic toughness ratios are qualitative because of the lack of available experimental data.

fracture (crack penetration mode) may be energetically preferred even under quasi-static loading, as indicated by the area where the dashed curved line is below the horizontal cross-hatched line in Fig. 4b. Note that the transgranular fracture generally covers a smaller range of interfacial angle for small quasi-static toughness ratios, suggesting that transgranular fracture should be relatively rare in such systems. This agrees with our SEM observations of only occasional transgranular fracture under the quasi-static loading condition.

For the dynamic case, the dynamic failure mode transition along well-controlled interfaces has been studied by Xu et al. [35], and their analysis is used as a baseline for modeling the dynamic intergranular–transgranular transition. Here we define  $G_d^{int}(\beta, v_2)$  and  $G_d^{Tra}(v_1)$  as the dynamic energy release rates of the intergranular fracture (deflected) crack tip and the transgranular fracture (penetrated) crack tip, respectively. Now the two dynamic energy release rates are not only a function of the interfacial angle  $\beta$ , but also a function of the incoming crack velocity  $v_1$  and the interfacial crack velocity  $v_2$ , as indicated in Fig. 4a.

Generally, the dynamic toughness of a homogeneous solid is a function of crack velocity  $v$  [36]. Kobayashi and Mall [37] measured the dynamic toughness of Homalite-100 (sometimes considered a prototypical brittle material in dynamic fracture experiments) as a function of crack velocity  $v$  and found that  $K_{ID}$  (dynamic fracture toughness) was almost equal to  $K_{IC}$  up to  $0.32c_R$ , where  $c_R$  is the Rayleigh wave speed. For the current AlN material, the crack speed was measured to be about  $1500 \text{ m s}^{-1}$ , around  $0.25c_R$ , from the in situ visualization [18]. Therefore, since the crack speeds are less than  $0.3c_R$ , the dynamic toughness of AlN is assumed to be equal to the quasi-static toughness ( $\Gamma_{cd}^{AlN} = \Gamma_c^{AlN}$ ); that is, we assume the dynamic toughness of the AlN grains to be independent of crack velocity for these velocities (and by extension independent of strain rate for these strain rates).

For the dynamic interfacial toughness  $\Gamma_{cd}^{IT}(v_2)$ , Xu et al. [35] argue that the interface toughness should be independent of crack velocity because of the suppression of microbranching along the well-controlled weak path. However, in many real material systems, due to the variation of interfacial toughness [33], the microbranching mechanism (small cracks in the grains) is actually operative. Further, computational analysis of the dynamic crack propagation along the interface suggests the dynamic toughness of the interface can increase dramatically at higher phase angles [34] and higher crack velocities [38]. Therefore, in the current analysis,  $\Gamma_{cd}^{IT}(v_2)$  is assumed to be an increasing function of interfacial crack velocity  $v_2$ .

A criterion for intergranular–transgranular transition under dynamic loading can now be formulated by incorporating the crack velocity dependence [35]

$$\frac{G_d^{int}(\beta, v_2)}{G_d^{Tra}(v_1)} \geq \frac{\Gamma_{cd}^{IT}(v_2)}{\Gamma_c^{AlN}} \quad (2a)$$

for intergranular fracture and

$$\frac{G_d^{int}(\beta, v_2)}{G_d^{Tra}(v_1)} < \frac{\Gamma_{cd}^{IT}(v_2)}{\Gamma_c^{AlN}} \quad (2b)$$

for transgranular fracture. Eqs. (2a) and (2b) is similar to Eqs. (1a) and (1b) in form, but with crack velocity dependence of energy release rates and the interfacial toughness. If criterion (2a) is satisfied, the crack tends to develop into intergranular fracture mode, and if criterion (2b) is satisfied, the crack tends to develop into transgranular fracture. Note that the ratio of the dynamic energy release rates  $G_d^{int}(\beta, v_2)/G_d^{Tra}(v_1)$  is maximized as the interfacial crack velocity  $v_2 \rightarrow 0$  for fixed  $\beta$  and  $v_1$ . Here we set  $G_d^{int}(\beta, v_2)/G_d^{Tra}(v_1)$  as  $G_d^{int}(\beta, 0)/G_d^{Tra}(v_1)$ . Since the left-hand side of Eqs. (2a) and (2b) is maximized, we can understand the upper bound of behavior (in terms of intergranular fracture). In Fig. 4b,  $G_d^{int}(\beta, 0)/G_d^{Tra}(v_1)$  is plotted against the interfacial angle  $\beta$  as a solid red curve, for the specific case of  $v_1 = 0.25c_R$  (measured crack velocity [18]). If we increase the interfacial crack velocity  $v_2$ , the ratio  $G_d^{int}(\beta, v_2)/G_d^{Tra}(v_1)$  will decrease. This trend is indicated by the arrow in Fig. 4b, and the dashed red curve is a schematic energy release ratio as a function of interfacial angle  $\beta$  when  $v_1 = 0.25c_R$  and  $v_2 > 0$ .

On the right-hand side of Eqs. (2a) and (2b), the dynamic toughness ratio  $\Gamma_{cd}^{IT}(v_2)/\Gamma_c^{AlN}(v_1)$  is a material property depending on the interfacial crack propagation velocity  $v_2$ . As noted above, the interface toughness  $\Gamma_{cd}^{IT}(v_2)$  increases as a function of crack velocity  $v_2$ , whereas  $\Gamma_c^{AlN}$  is constant. This leads to the upward shift of the dynamic toughness ratio under dynamic loading conditions (as compared to the quasi-static case). This trend is indicated by the green arrow, and an example of the dynamic toughness ratio is represented as the horizontal solid red line in Fig. 4b. The intercept of dynamic energy release ratio and dynamic toughness ratio determines the relative likelihood of transgranular fracture versus intergranular fracture, as governed by Eqs. (2a) and (2b) and indicated in Fig. 4b. It is evident that, under dynamic loading conditions, the transgranular region must increase because of the dynamic fracture mechanics. Note that if the interfacial crack velocity  $v_2$  increases, the energy release rate ratio will continue to decrease and the dynamic toughness ratio will continue to increase, resulting in an even higher percentage of transgranular fracture. We thus have a mechanistic understanding of why transgranular fracture is more likely at high strain rates.

This leads to the question of the strain rate that controls this intergranular fracture  $\rightarrow$  transgranular fracture transition. To estimate this, we must relate the crack velocity to the strain rate. A simple conceptual argument is as follows. In one-dimensional terms, the stress and strain relationship of brittle materials can be expressed as

$$\sigma = E\varepsilon = E\dot{\varepsilon}t \quad (3)$$

where  $\sigma$  is the stress,  $E$  is the Young's modulus,  $\varepsilon$  is the strain,  $\dot{\varepsilon}$  is the constant strain rate and  $t$  is the time. The

stress intensity factor (SIF)  $K_I$  can be expressed as (for mode I cracks)

$$K_I = \alpha \sigma \sqrt{\pi l} \quad (4)$$

where  $l$  is half of the crack length and  $\alpha$  is a corrector factor depending on the loading and geometry.  $\alpha$  is generally around 1. The SIF can be related with the energy release rate under plane strain conditions through

$$G = \frac{1 - \nu^2}{E} K_I^2 \quad (5)$$

where  $G$  is the energy release rate and  $\nu$  is Poisson's ratio. When

$$G = \Gamma_c(v) \quad (6)$$

cracks begin to grow, where  $\Gamma_c(v)$  is the dynamic fracture toughness (which is a function of crack velocity as noted above). Then the stress can be rearranged in terms of  $\Gamma_c(v)$  and  $l$  as

$$\sigma = \sqrt{\frac{\Gamma_c(v)E}{(1 - \nu^2)\alpha^2\pi l}} \quad (7)$$

The crack length  $l$  and (constant) crack velocity  $v$  are related through

$$l = vt \quad (8)$$

Now we can relate Eqs. (3), (7), and (8) to obtain a scaling relationship between the strain rate  $\dot{\epsilon}$  and crack velocity  $v$ .

$$\dot{\epsilon} = \frac{1}{\alpha\sqrt{\pi E(1 - \nu^2)}} \frac{v\sqrt{\Gamma_c(v)}}{l^{3/2}} \quad (9)$$

As noted above,  $\Gamma_c(v)$  is a non-decreasing function of crack velocity  $v$ . Eq. (9) shows that higher crack velocities correspond to higher strain rates. For polycrystalline materials, we assume that the crack length  $l$  is a multiple of the grain size  $d$ .

In Fig. 4b, as noted above, the intercept between the dynamic toughness ratio and the dynamic energy release rate ratio determines the boundary of intergranular and transgranular fracture under dynamic loading. We define the “transitional crack velocity”  $v_t$  as the crack velocity at which intergranular and transgranular fracture are equally possible. Assuming the random orientation (distribution) of the grains, the transitional crack velocity  $v_t$  is approximately the velocity at which the dynamic toughness ratio intercepts the dynamic energy release rate ratio at interfacial angles of about  $\beta = \pi/4$ . From Fig. 4b, if we know the value of the dynamic toughness ratio and are given the interfacial crack velocity  $v_2$ , we can equate the maximized energy release rate ratio at  $\beta = \pi/4$  with the dynamic toughness ratio to solve for the transitional crack velocity  $v_t$ , and then the crack velocity  $v_t$  will be expressed as the following function:

$$v_t = g \left\{ \frac{\Gamma_{cd}^{IT}(v_2)}{\Gamma_c^{AIN}}, \frac{G_d^{int}(45^\circ, 0)}{G_d^{tra}(v_t)} \right\} \quad (10)$$

Note that the  $v_t$  estimated above will provide an upper estimate for the transitional crack velocity, because the maxi-

mized energy release rate ratio ( $\beta = 45^\circ$ ,  $v_2 = 0$ ) is utilized. Given this transitional velocity, we can determine the transitional strain rate as the strain rate at which the transgranular fracture becomes more likely than intergranular fracture. Substituting the transitional crack velocity  $v_t$  into Eq. (9), we compute the transitional strain rate as

$$\dot{\epsilon} = \frac{1}{\alpha\sqrt{\pi E(1 - \nu^2)}} \frac{v_t\sqrt{\Gamma(v_t)}}{l^{3/2}} \quad (11)$$

For the current AlN, the experimental value for the dynamic toughness ratio  $\Gamma_{cd}^{IT}(v_2)/\Gamma_c^{AIN}$  is not known, but is presumed to be of order 1. The transitional crack velocity  $v_t$  can be obtained by numerical solution of Eq. (10) as  $v_t = 1450$  m/s. The crack length  $2l$  is assumed to be 10–100 times the grain size ( $2l \approx 50 \sim 500 \mu\text{m}$  in this case; the minimum crack length that can be resolved by our high-speed camera is about  $500 \mu\text{m}$ ). Further, we have  $K_{IC} = 2.7 \text{ MPa}\sqrt{\text{m}}$ ,  $E = 320 \text{ GPa}$ ,  $\nu = 0.237$ ,  $\alpha = 1$ , and using Eq. (11) gives us an estimation of the transitional strain rate on the order of  $10^3$ – $10^4 \text{ s}^{-1}$ . Note that this is an upper estimate. Our observations of primarily transgranular fracture at strain rates of  $10^3 \text{ s}^{-1}$  are consistent with this analysis. The analysis also indicates that the transition should occur at approximate these rates for all polycrystalline advanced ceramics, since the characteristic properties ( $K_{IC}$ ,  $E$ , etc.) have similar orders of magnitude. This is also consistent with the observations in the literature.

#### 4.2. Modeling confining stress effects on fracture mechanisms

The effects of confining stress on yttria failure can be understood through wing crack micromechanics [39,40]. Under plane strain conditions, when the brittle solid experiences a uniaxial compressive load  $\sigma_1$ , the potential defects become active and form wing cracks, tending to align themselves along the loading direction. However, if a confining stress  $\sigma_2$  is applied, it will decrease the stress intensity factor  $K_I$  at the crack tip. With an increase of  $\sigma_2$ , the stress intensity factor  $K_I$  at the crack tip will finally go to zero. At this time, the cracking mechanism is entirely shut down, and the magnitude of  $\sigma_2$  to achieve the shut-down is only dependent on the internal friction coefficient  $\mu$  through the following relationship [18]:

$$\sigma_2 = \frac{(1 + \mu^2)^{1/2} - \mu}{(1 + \mu^2)^{1/2} + \mu} \sigma_1 \quad (12)$$

With  $\mu = 0.4$  [41] and  $\sigma_1 = 4 \text{ GPa}$ , taken as the strength of AlN,  $\sigma_2$  can be calculated as  $1.8 \text{ GPa}$ . Once the cracking mechanism is shut down, other mechanisms, such as dislocations and twinning, are needed to accommodate the deformation of the solid.

The yield strength can be estimated from  $\sigma_y = H/\alpha$ , where  $H$  is the hardness and  $\alpha$  is a constant (generally 3.0 for metals [42] and 2.1 for ceramics [43]). For yttria, the hardness is about  $8.8 \text{ GPa}$  [44] and the yield strength is around  $4 \text{ GPa}$ ; for AlN, the hardness is  $17.7 \text{ GPa}$  [45]

and the yield strength is around 8 GPa. The lower yield strength of yttria suggests that it should yield first once the cracking mechanism is shut down. Indeed, dislocations in yttria are confirmed through TEM observations below (shown in Fig. 6). After the interphase yields, the yielding sites (typically the triple junctions, illustrated in Fig. 2a) will act as new defects triggering the subsequent crack formation. This is similar to the Berkovich indentation scenario, in which tensile stresses can be generated around the indentation sites, leading to cone cracks [46]. In the current experimental condition, the confining stress is not large enough to shut down all cracks. However, due to the inhomogeneities in the brittle material, the confining stress level appears to be large enough to trigger some yttria failure. Furthermore, we observe the trend that the

probability of observing yttria failure increases with increasing confining stress, consistent with this analysis.

#### 4.3. Fracture mechanism summary for sintered AlN

The strain rate and confining stress are critical variables in dynamic loading applications. Based upon our observations and previous modeling discussion, the fracture mechanism for sintered AlN can be summarized as follows. At low strain rate and low confining stress, corresponding to the quasi-static uniaxial compression tests, intergranular fracture is dominant. With an increase in the strain rate at similar low confining stresses, transgranular fracture becomes dominant. As the confining stress is increased, the interphase failure mechanism becomes active, and for

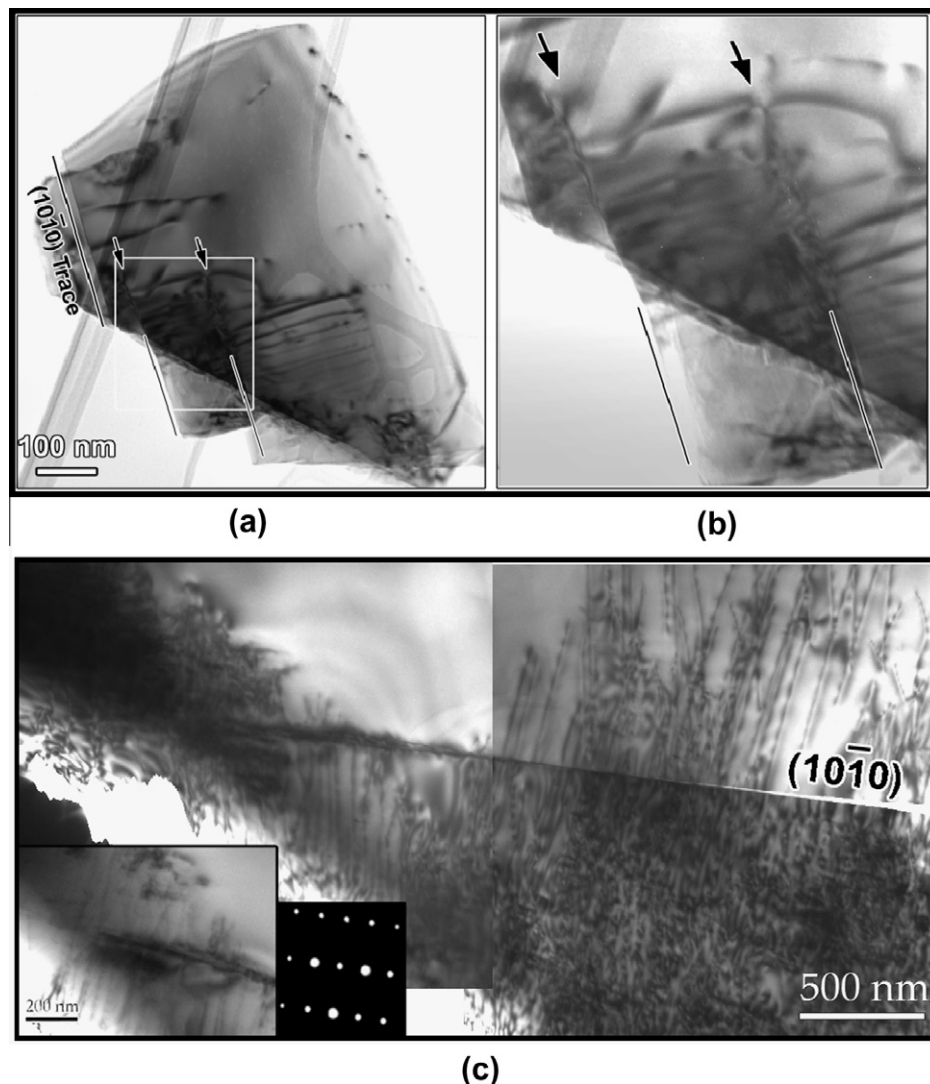


Fig. 5. Bright-field TEM observations of collected fragments from a specimen dynamically tested at a 780 MPa confining stress, showing AlN microcrystals produced from fragmented AlN grains as a result of the interphase and transgranular fracture. (a) Global picture of a small AlN fragment contains several groups of dislocations, each group showing a planar slip characteristic, associated with a well-defined cleavage facet at the edge. (b) Close-up observation of the framed area in (a) with arrows annotating the microcrack tips. (c) Micrograph capturing the transgranular crack being arrested in the interior of the crystal, with profuse dislocations associated with the present microcrack, either along the crack path or at the crack tip. The insets in (c) are a zoom-in view of the crack tip being stopped in the crystal and selected area electron diffraction of the AlN crystal.



higher confining stresses, more interphase failure is observed. Note that no experiments were conducted at low strain rates and high confining stresses. The fracture mode in this loading regime is predicted to be a combination of intergranular fracture and interphase failure based upon the modeling efforts. This fracture mechanism study has significant material design implications. For example, if a material is designed to be in service under a low strain rate condition, grain boundary engineering should be the most important factor; on the other hand, if it is designed for impact applications involving high confinement and high strain rates, the effects of grain strength and second (inter-) phases could have a larger impact on the performance.

### 5. Brittle to ductile transition mechanisms

The experimental results from various experimental techniques on AlN were summarized in a deviatoric strength and hydrostatic pressure space by Hu et al. [18], who demonstrated that there exists a transition pressure ( $\sim 2$  GPa) at which a shift from brittle to ductile behavior is observed. Below the transition pressure, pre-existing defects dominate the material response, which can be modeled and predicted using the wing-crack micromechanics model; this is therefore called the defect controlled region [18]. As the pressure increases, the cracking mechanism is suppressed due to the corresponding decrease of the stress intensity factor  $K_I$  at crack tips [39,47,48]. Thus other mechanisms, such as dislocation activity, become viable. This is substantiated both by the macroscopic experimental data, showing (above the transition pressure) the insensitivity of the deviatoric strength to pressure, and by the microscopic observation of dislocations. We provide detailed microscopic evidence for the “dislocation controlled region” in this section.

Specimens after quasi-static, uniaxial dynamic and confined dynamic experiments with different confining stresses were examined by TEM. Multiple specimens were observed for each test to obtain representative microstructural information. In both quasi-statically and dynamically compressed specimens under uniaxial load, dislocations were rarely observed. This is consistent with the observation that these specimens fail through brittle fracture. However, the specimens subjected to confined dynamic tests showed different characteristics. Deformation under confined dynamic compression produces a large number of fragments in the form of fine powders. These fragments can be extremely small and thin, e.g. a few microns wide and less than 100 nm thick. They are thin enough to be electron beam transparent and immediately ready for TEM observations.

In striking contrast to specimens tested under uniaxial loading, large numbers of dislocations were observed in specimens tested through the confined dynamic loading procedure. Dislocations were present in almost every fragment produced during the failure process. Generally, an AlN fragment is not a whole grain, but only a section of it due to the transgranular failure. An example of an AlN

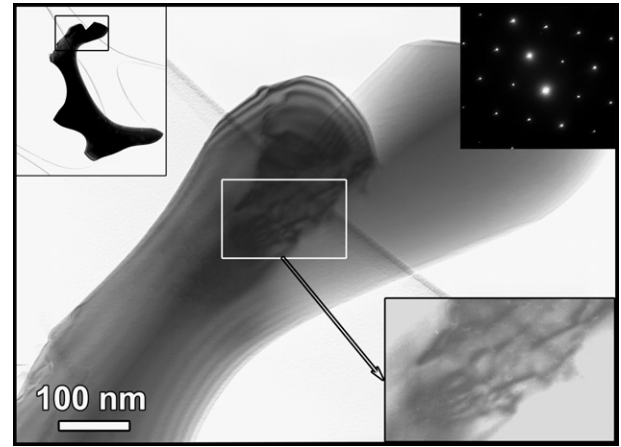


Fig. 6. Bright-field TEM observations of collected fragments from a specimen dynamically tested at a 780 MPa confining stress showing a zoom-in view of an yttria interphase fragment detached from AlN grains as a result of interphase failure. The top-left inset is a global picture of the yttria phase, with the frame defining the area where the picture is taken; the top-right inset shows the diffraction pattern of the fragment. Dislocations are clearly observable in the inset at the bottom, which is a zoom-in view of the framed area in the main picture.

fragment is shown in Fig. 5a. This small AlN fragment contains several groups of dislocations, each group showing a planar slip characteristic lying on the trace of the prismatic ( $10\bar{1}0$ ) plane. A series of tilting experiments with different dual beam conditions suggests a Burgers vector of  $1/3[11\bar{2}0]$ , indicating the prismatic  $\langle a \rangle$ -type slip. This slip system is common in hexagonal structures with a  $c/a$  ratio smaller than the ideal value of 1.633, where the most closely packed plane is the prismatic plane. This slip system was also reported by others [1,8–11,49].

Cleavage facets on ( $10\bar{1}0$ ) plane are generally observed on the edges of the AlN fragments, consistent with one of the most readily available cleavage planes in wurtzite crystal structure [20] (note this is also one of the available slip planes). It can be seen from Fig. 5a and the close-up observation shown in Fig. 5b that each cleavage facet is associated with a particular group of dislocations located near the edge of the fragmented crystal. Each group of dislocations lies on a trace which is an extension of the cleavage facet into the microcrystal, suggesting inherent correlation between the dislocations and microcracking. These observations are further confirmed by the micrograph shown in Fig. 5c, which captures a “propagating” microcrack observed within another AlN fragment and provides details on the correlation between microcracking and dislocation activities. The zone axis is also along the  $[11\bar{2}0]$  direction (same as in Fig. 5a). Several interesting features of the microcrack can be observed. First, it is clearly seen that the microcrack stops in the interior of the grain, with the crack tip clearly observable (see the bottom inset). Second, the microcrack is associated with large numbers of dislocations either along the crack path or at the crack tip. Third, the crack is straight and the crack surface is flat, characteristic of typical cleavage surfaces. Finally, there

appears to be something like a cohesive zone behind the crack tip about 2  $\mu\text{m}$  in length, where there is no crack opening displacement and the deformation is typical of a highly localized slip band.

These observations are consistent with the observations of Fig. 5a and b, and provide important information for understanding the deformation mechanisms. The slip band ahead of the “propagating” microcrack indicates that the opening of the crack is preceded by the slip deformation. This suggests an important role of dislocations in the microcracking process since slip is accommodated by gliding of dislocations. Note that, in comparison to the major cracks that produced the fragments, the microcracks retained and observed in the fragments are quite minor cracks. Together with the multiple cracking suggested by multiple cleavage facets in Fig. 5a and b, we speculate that a considerable number of relatively minor cracks can be formed during the propagation of the main crack, serving as another mechanism to dissipate energy during the dynamic deformation under high confining stresses. Such multiple cracks associated with dislocations are not observed in specimens tested under uniaxial loading conditions.

In brittle materials, cleavage is generally a mechanism that does not rely on dislocation activities. However, the observations here suggest that, under some conditions, e.g. a confined dynamic loading, cleavage following the prismatic plane could be closely associated with dislocation behaviors. The cohesive zone at the crack tip, characterized by the intense slip rather than an opening mode, suggests that dislocations could act as a precursor to the crack opening. It is quite possible that the dislocations are generated during the loading regime, leading to high strain (stress) concentration. When the loading is released, the microcracks (cleavage) may be induced at these stress concentration sites (generally the highly slipped regions).

With increasing confining pressure and strain rate, it is therefore to be expected that the flaw-controlled brittle fracture is increasingly dominated by dislocation behaviors. Above a critical pressure, a brittle to ductile transition will occur as a result of the extreme loading conditions. The microscopic observations in the fine fragments here further demonstrate the existence of profuse dislocations interacting with microcracks at a much smaller length scale, substantiating the brittle to ductile transition obtained from macroscopic strength data of AlN.

The existence of a large number of microcracks and the remarkable associated dislocation behavior suggest that complex interactions between brittle cracking and dislocation-mediated plasticity coexist in this system under confined dynamic loading. The cooperation of flaw-controlled cracking and dislocation-mediated plasticity probably mean that the classic Griffith criterion for brittle materials needs to be modified to describe this type of material behavior.

In addition to the fragmented AlN microcrystals, individual yttria phases detached from AlN grains are also

often observed, consistent with the SEM observation of interphase failure at high confinement. An example of the deformed yttria phase is shown in Fig. 6. The yttria phase can be readily recognized through the morphology (top left inset), and is further confirmed through diffraction patterns (top right inset) or elemental analysis. This ceramic phase also experiences noticeable local plastic deformation, as a number of dislocations were present, shown in the bottom inset in Fig. 6, suggesting another microscopic energy dissipation mechanism besides interphase boundary decohesion.

## 6. Summary

Uniaxial quasi-static, uniaxial dynamic and confined dynamic tests on sintered AlN were performed. Extensive SEM and TEM characterization of fragments were conducted to identify fracture and deformation mechanisms at different loading conditions. Our primary conclusions follow.

- Intergranular fracture is the dominant fracture mechanism in sintered AlN at low strain rates and low confining stresses. With the increase of the strain rate, transgranular fracture becomes dominant, with a transitional strain rate defined by the dynamic failure mechanics. At high strain rates with high confining stress, interphase failure becomes viable, along with intergranular and transgranular fracture.
- Dynamic fracture mechanics is used to explain the intergranular fracture to transgranular fracture transition under different loading rates, while wing-crack micromechanics is recalled to explain the interphase failure with increasing confining stress.
- The deformation mechanisms of AlN change with pressure. The transition is substantiated both by macroscopic strength data and microscopic observations. Both fracture and dislocation activities exist around the transition pressure regime.
- TEM characterization of specimens tested at different loading conditions not only confirmed the existence of dislocation mechanisms under confined dynamic loading, but also revealed microcrack–dislocation interactions at small length scales, implying that the plasticity affects the material behavior to a significant extent.

## Acknowledgements

This work was performed under the auspices of the Center for Advanced Metallic and Ceramic Systems at the Johns Hopkins University, supported by Army Research Laboratory under the REDCOM-ACQ-CTR Cooperative Agreement No. W911NF-06-2-0006. Helpful discussions with Dr. Cao, Dr. Daphalapurkar and Dr. Kimberley are greatly appreciated.



## References

- [1] Denanot MF, Rabier J. *J Mater Sci* 1989;24:1594.
- [2] Yonenaga I, Shima T, Sluiter MHF. *Jpn J Appl Phys* 2002;41:4620.
- [3] McNeil LE, Grimsditch M, French RH. *J Am Ceram Soc* 1993;76:1132.
- [4] German RM. *Liquid phase sintering*. New York: Plenum Press; 1985.
- [5] Heard H, Cline C. *J Mater Sci* 1980;15:1889.
- [6] Delavignette P, Amelinckx S, Kirkpatrick HB. *J Appl Phys* 1961;32:1098.
- [7] Blank H, Delavignette P, Amelinckx S. *Phys Status Solidi (B)* 1962;2:1660.
- [8] Seifert A, Berger A, Muller WF. *J Am Ceram Soc* 1992;75:873.
- [9] Audurier V, Demenet JL, Rabier J. *Mater Sci Eng A* 1993;164:360.
- [10] Audurier V, Demenet JL, Rabier J. *Philos Mag A* 1998;77:825.
- [11] Audurier V, Demenet JL, Rabier J. *Philos Mag A* 1998;77:843.
- [12] Chen WN, Ravichandran G. *J Am Ceram Soc* 1996;79:579.
- [13] Subhash G, Ravichandran G. *J Mater Sci* 1998;33:1933.
- [14] Rosenberg Z, Brar NS, Bless SJ. *J Appl Phys* 1991;70:167.
- [15] Dandekar DP, Abbate A, Frankel J. *J Appl Phys* 1994;76:4077.
- [16] Kipp ME, Grady DE. *EURODYMAT* 1994;94:249.
- [17] Chen W, Ravichandran G. *Int J Fract* 2000;101:141.
- [18] Hu G, Ramesh KT, Cao B, McCauley JW. *J Mech Phys Solids* 2011;59:1076.
- [19] Andrievski RA, Kalinnikov GV, Jauberteau J, Bates J. *J Mater Sci* 2000;35:2799.
- [20] Adachi S. *Properties of group-IV, III-V and II-VI semiconductors*. Chichester: John Wiley & Sons Ltd; 2005.
- [21] Suzuki TS, Uchikoshi T, Sakka Y. *J Eur Ceram Soc* 2009;29:2627.
- [22] Paliwal B, Ramesh KT, McCauley JW, Chen MW. *J Am Ceram Soc* 2008;91:3619.
- [23] Espinosa HD, Raiser G, Clifton RJ, Ortiz M. *J Hard Mater* 1992;3:285.
- [24] Rafaniello W, Zhao J, Haney C. Personal communication.
- [25] Salem J, Ghosn L. *Int J Fract* 2010;164:319.
- [26] Yang K-H, Kobayashi AS. *J Am Ceram Soc* 1990;73:2309.
- [27] Hu G, Chen CQ, Ramesh KT, McCauley JW. *Scripta Mater* 2012;66:527.
- [28] Kraft RH, Molinari JF, Ramesh KT, Warner DH. *J Mech Phys Solids* 2008;56:2618.
- [29] Zavattieri PD, Espinosa HD. *Acta Mater* 2001;49:4291.
- [30] Yang W-J, Yu C-T, Kobayashi AS. *J Am Ceram Soc* 1991;74:290.
- [31] Belenky A, Bar-On I, Rittel D. *J Mech Phys Solids* 2010;58:484.
- [32] Spanoudakis J, Young R. *J Mater Sci* 1984;19:487.
- [33] German RM, Hanafee JE, Digiallonardo SL. *Metall Mater Trans A* 1984;15:121.
- [34] Hutchinson JW, Suo Z. *Adv Appl Mech* 1992;29.
- [35] Roy Xu L, Huang Y, Rosakis AJ. *J Mech Phys Solids* 2003;51:461.
- [36] Ravi-Chandar K. *Dynamic fracture*. Austin, TX: Elsevier; 2004.
- [37] Kobayashi A, Mall S. *Exp Mech* 1978;18:11.
- [38] Lo CY, Nakamura T, Kushner A. *Int J Solids Struct* 1994;31:145.
- [39] Ashby MF, Hallam SD. *Acta Metall* 1986;34:497.
- [40] Horii H, Nemat-Nasser S. *J Geophys Res* 1985;90.
- [41] Tkachenko YG, Yulyugin VK, Dubovik TV. *Powder Metall Met Ceram* 1983;22:405.
- [42] Nix WD, Gao H. *J Mech Phys Solids* 1998;46:411.
- [43] Gilman JJ. *J Appl Phys* 1975;46:1435.
- [44] Albayrak IC, Basu S, Sakulich A, Yeheskel O, Barsoum MW. *J Am Ceram Soc* 2010;93:2028.
- [45] Yonenaga I, Nikolaev A, Melnik Y, Dmitriev V. *Jpn J Appl Phys Lett* 2001;40:L426.
- [46] Zeng K, Giannakopoulos AE, Rowcliffe D, Meier P. *J Am Ceram Soc* 1998;81:689.
- [47] Horii H, Nemat-Nasser S. *Phil Trans R Soc Lond A* 1986:319.
- [48] Tapponnier P, Brace WF. *Int J Rock Mech Min Sci* 1976;13:103.
- [49] Masson I, Feiereisen JP, Michel JP, George A, Mocellin A, Blumenfeld P. *J Eur Ceram Soc* 1994;13:355.

NO. OF  
COPIES ORGANIZATION

1 DEFENSE TECHNICAL  
(PDF INFORMATION CTR  
only) DTIC OCA  
8725 JOHN J KINGMAN RD  
STE 0944  
FORT BELVOIR VA 22060-6218

1 DIRECTOR  
US ARMY RESEARCH LAB  
IMNE ALC HRR  
2800 POWDER MILL RD  
ADELPHI MD 20783-1197

1 DIRECTOR  
US ARMY RESEARCH LAB  
RDRL CIO LL  
2800 POWDER MILL RD  
ADELPHI MD 20783-1197

NO. OF  
COPIES ORGANIZATION

1 PEO GCS  
SFAE GCS BCT/MS 325  
M RYZYI  
6501 ELEVEN MILE RD  
WARREN MI 48397-5000

1 ABRAMS TESTING  
SFAE GCSS W AB QT  
J MORAN  
6501 ELEVEN MILE RD  
WARREN MI 48397-5000

1 COMMANDER  
WATERVLIET ARSENAL  
SMCWV QAE Q  
B VANINA  
BLDG 44  
WATERVLIET NY 12189-4050

1 COMMANDER  
US ARMY AMCOM  
AVIATION APPLIED TECH DIR  
J SCHUCK  
FT EUSTIS VA 23604-5577

1 USA SBCCOM PM SOLDIER SPT  
AMSSB PM RSS A  
J CONNORS  
KANSAS ST  
NATICK MA 01760-5057

1 UNIV OF DELAWARE  
DEPT OF MECH ENGR  
J GILLESPIE  
NEWARK DE 19716

3 AIR FORCE ARMAMENT LAB  
AFATL DLJW  
D BELK  
J FOSTER  
W COOK  
EGLIN AFB FL 32542

1 TACOM ARDEC  
AMSRD AAR AEE W  
E BAKER  
BLDG 3022  
PICATINNY ARSENAL NJ  
07806-5000

NO. OF  
COPIES ORGANIZATION

11 US ARMY TARDEC  
AMSTRA TR R MS 263  
K BISHNOI  
D TEMPLETON (10 CPS)  
WARREN MI 48397-5000

1 COMMANDER  
US ARMY RSRCH OFC  
A RAJENDRAN  
PO BOX 12211  
RSRCH TRIANGLE PARK NC  
27709-2211

2 CALTECH  
G RAVICHANDRAN  
T AHRENS MS 252 21  
1201 E CALIFORNIA BLVD  
PASADENA CA 91125

5 SOUTHWEST RSRCH INST  
C ANDERSON  
K DANNEMANN  
T HOLMQUIST  
G JOHNSON  
J WALKER  
PO DRAWER 28510  
SAN ANTONIO TX 78284

3 SRI INTERNATIONAL  
D CURRAN  
D SHOCKEY  
R KLOOP  
333 RAVENSWOOD AVE  
MENLO PARK CA 94025 21

1 APPLIED RSRCH ASSOCIATES  
D GRADY  
4300 SAN MATEO BLVD NE  
STE A220  
ALBUQUERQUE NM 87110

1 INTERNATIONAL RSRCH  
ASSOCIATES INC  
D ORPHAL CAGE 06EXO  
5274 BLACKBIRD DR  
PLEASANTON CA 94566

1 BOB SKAGGS CONSULTANT  
S R SKAGGS  
7 CAMINO DE LOS GARDUNOS  
SANTA FE NM 87506

NO. OF  
COPIES ORGANIZATION

2 WASHINGTON ST UNIV  
INST OF SHOCK PHYSICS  
Y GUPTA  
J ASAY  
PULLMAN WA 99164-2814

1 COORS CERAMIC CO  
T RILEY  
600 NINTH ST  
GOLDEN CO 80401

1 UNIV OF DAYTON  
RSRCH INST  
N BRAR  
300 COLLEGE PARK  
MS SPC 1911  
DAYTON OH 45469-0168

1 COMMANDER  
US ARMY TACOM  
AMSTA TR S  
L PROKURAT FRANKS  
WARREN MI 48397-5000

1 PM HBCT  
SFAE GCS HBCT S  
J ROWE MS 506  
6501 11 MILE RD  
WARREN MI 48397-5000

3 COMMANDER  
US ARMY RSRCH OFC  
B LAMATINA  
D STEPP  
W MULLINS  
PO BOX 12211  
RSRCH TRIANGLE PARK NC  
27709-2211

1 NAVAL SURFACE WARFARE CTR  
CARDEROCK DIVISION  
R PETERSON  
CODE 28  
9500 MACARTHUR BLVD  
WEST BETHESDA MD 20817-5700

2 LAWRENCE LIVERMORE NATL LAB  
R LANDINGHAM L369  
J E REAUGH L282  
PO BOX 808  
LIVERMORE CA 94550

NO. OF  
COPIES ORGANIZATION

3 SANDIA NATL LAB  
J ASAY MS 0548  
L CHHABILDAS MS 0821  
D CRAWFORD ORG 0821  
PO BOX 5800  
ALBUQUERQUE NM 87185-0820

1 RUTGERS  
THE STATE UNIV OF NEW JERSEY  
DEPT OF CRMCS & MATLS ENGRNG  
R HABER  
607 TAYLOR RD  
PICATINNY NJ 08854

1 THE UNIVERSITY OF TEXAS  
AT AUSTIN  
S BLESS  
IAT  
3925 W BRAKER LN STE 400  
AUSTIN TX 78759-5316

1 CERCOM  
R PALICKA  
1960 WATSON WAY  
VISTA CA 92083

6 GDLS  
W BURKE MZ436 21 24  
G CAMPBELL MZ436 30 44  
D DEBUSSCHER MZ436 20 29  
J ERIDON MZ436 21 24  
W HERMAN MZ435 01 24  
S PENTESCU MZ436 21 24  
38500 MOUND RD  
STERLING HTS MI 48310-3200

1 JET PROPULSION LAB  
IMPACT PHYSICS GROUP  
M ADAMS  
4800 OAK GROVE DR  
PASADENA CA 91109-8099

3 OGARA HESS & EISENHARDT  
G ALLEN  
D MALONE  
T RUSSELL  
9113 LE SAINT DR  
FAIRFIELD OH 45014

NO. OF  
COPIES ORGANIZATION

1 CERADYNE INC  
M NORMANDIA  
3169 REDHILL AVE  
COSTA MESA CA 96626

2 JOHNS HOPKINS UNIV  
DEPT OF MECH ENGRNG  
K T RAMESH  
T W WRIGHT  
3400 CHARLES ST  
BALTIMORE MD 21218

2 SIMULA INC  
V HORVATICH  
V KELSEY  
10016 51ST ST  
PHOENIX AZ 85044

3 UNITED DEFENSE LP  
K STRITTMATTER  
E BRADY  
R JENKINS  
PO BOX 15512  
YORK PA 17405-1512

10 NATL INST OF STANDARDS & TECH  
CRMCS DIV  
G QUINN  
STOP 852  
GAITHERSBURG MD 20899

2 DIR USARL  
RDRL D  
C CHABALOWSKI  
V WEISS  
2800 POWDER MILL RD  
ADELPHI MD 20783-1197 23

ABERDEEN PROVING GROUND

60 DIR USARL  
RDRL SL  
R COATE  
RDRL WM  
S KARNA  
P BAKER  
J MCCAULEY (10 CPS)  
RDRL WML  
J NEWILL  
M ZOLTOSKI  
RDRL WML B  
D TAYLOR (10 CPS)  
RDRL WMM  
R DOWDING

NO. OF  
COPIES ORGANIZATION

RDRL WMM A  
J SANDS  
T WEERASOORIYA  
RDRL WMM D  
E CHIN  
K CHO  
G GAZONAS  
R SQUILLACIOTI  
RDRL WMM E  
J LASALVIA  
P PATEL  
RDRL WMM F  
J MONTGOMERY  
RDRL WMP  
B BURNS  
S SCHOENFELD  
RDRL WMP B  
C HOPPEL  
M SCHEIDLER  
RDRL WMP C  
T BJERKE  
J CLAYTON  
D DANDEKAR  
M GREENFIELD  
S SEGLETES  
W WALTERS  
RDRL WMP D  
T HAVEL  
M KEELE  
D KLEPONIS  
H MEYER  
J RUNYEON  
RDRL WMP E  
P BARTKOWSKI  
M BURKINS  
W GOOCH  
D HACKBARTH  
E HORWATH  
T JONES  
RDRL WML H  
T FARRAND  
L MAGNESS  
D SCHEFFLER  
R SUMMERS

INTENTIONALLY LEFT BLANK.